Geophysical Journal International

Geophys. J. Int. (2019) **219,** 995–1007
Advance Access publication 2019 July 26
GJI Seismology

doi: 10.1093/gji/ggz342

Source localization and joint velocity model building using wavefront attributes

Leon Diekmann,[1] Benjamin Schwarz,[2] Alexander Bauer[1] and Dirk Gajewski[1]

[1] *Institute of Geophysics, University of Hamburg, Bundesstrasse* 55, 20146 *Hamburg, Germany. E-mail: l.d.diekmann@uu.nl*
[2] *Department of Earth Sciences, University of Oxford, South Parks Road, Oxford OX*13*AN, United Kingdom*

Accepted 2019 July 25. Received 2019 July 17; in original form 2018 November 28

SUMMARY

The localization of passive seismic sources in form of microseismic tremors as well as large-scale earthquakes is a key issue in seismology. While most previous studies are assuming fairly good knowledge of the underlying velocity model, we propose an automatic spatial localization and joint velocity model building scheme that is independent of detailed *a priori* information. The first step is a coherence analysis, estimating so-called wavefront attributes to locally describe the wavefield in terms of slopes and curvatures. In a similar fashion, we also obtain an initial guess of the source excitation times of the recorded events. The wavefront attributes constitute the input for wavefront tomography which represents the next step of the workflow and allows for a refinement of the previously evaluated source excitation times while simultaneously approximating the velocity distribution. In a last step, we use the final estimate of the velocity distribution and compute the respective image function by reverse time modelling to gain the source locations. This paper introduces the theoretical concept of our proposed approach for the general 3-D case. We analyse the feasibility of our strategy and the influences of different acquisition settings by means of a synthetic 2-D data example. In a final 3-D field data example we use the workflow to localize a deep earthquake without relying on a given velocity model. The approach can deal with high levels of noise and low signal amplitudes, respectively, as well as sparse geophone sampling. The workflow generally delivers good approximations of the long-wavelength velocity variations along with accurate source locations.

Key words: Seismic tomography; Joint inversion; Induced seismicity; Earthquake source observations.

1 INTRODUCTION

A passive seismic source can be defined as an origin of energy located within the interior of the Earth. Once, the energy is released at the source it propagates through the Earth and eventually reaches the surface, where the ground motion is recorded by seismic receivers. Such events occur on all scales, for instance in form of large-amplitude earthquakes or faint tremors which can hardly be felt by humans. Those weak events are referred to as microseismicity and can be induced either naturally or anthropogenically. Natural tremors occur for instance related to pressure fluctuations in volcanic and geothermal areas (e.g. Aki *et al.* 1977). In the context of hydraulic fracturing, however, tremors are generated intentionally with the aim to enhance hydrocarbon extraction rates or improve the geothermal efficiency for sustainable power generation (Rubinstein & Mahani 2015). By injecting a pressurized fluid into a wellbore, cracks arise in the rock formation, allowing for an improved flow, for example of petroleum or gas when extracted (Suckale 2009). While this technique has had a notable impact on the energy sector, the unintentional triggering of earthquakes through a related change in the local stress regime can have unforeseen consequences and therefore remains at the centre of scientific and public attention (e.g. Ellsworth 2013; Segall & Lu 2015; Langenbruch & Zoback 2016). Monitoring aims at recording and localizing these cracks to improve and control the fracturing processes (e.g. Maxwell & Urbancic 2001; Li *et al.* 2019).

Thus, the localization of seismic sources is of fundamental importance. In general, one is confronted with a multidimensional mostly ill-posed inverse problem when studying earthquakes (e.g. Shearer 2019). While the stability and reliability of inversion techniques benefit from ever-improving and often dense instrumentation, the fact that wavefields are recorded almost exclusively on land and at the Earth's surface represents natural challenges that are hard to circumvent. As a result, there is a fundamental ambiguity between velocity structure and the location of an earthquake—an effect that

© The Author(s) 2019. Published by Oxford University Press on behalf of The Royal Astronomical Society.

Downloaded from https://academic.oup.com/gji/article-abstract/219/2/995/5539537 by Said Business School user on 23 September 2019

is often magnified by uncertainties in the estimation of source origin times (Kissling 1988; Thurber 1992). In addition to this so-called hypocentre–velocity coupling, a linearization of the inverse problem, which enables a computationally efficient implementation, results in an inherent dependence on a sufficiently accurate starting model in a least-squares framework (e.g. Kissling *et al.* 1994). Whereas powerful largely data-driven methods have been introduced for the estimation of the epicentre, that is the lateral location of an earthquake, the accurate determination of an earthquake's depth—in particular for very deep seismicity—remains a fundamental challenge that results from the restriction of measurement designs to the Earth's surface (Engdahl *et al.* 1998; Rost & Thomas 2002). Largely ignoring the hypocentre-velocity coupling, first approaches (re-)localize seismic events using pre-determined velocity models (e.g. Eaton 1970; Lee & Lahr 1972; Lienert *et al.* 1986; Lienert & Havskov 1995; Lomax *et al.* 2000). Also, a vast majority of these early approaches rely on the accurate picking of onset traveltimes, which makes them vulnerable to high noise levels. Owing to their stability, the aforementioned methods have had tremendous success and supplied catalogues that are still routinely used in practice (e.g. Kennett & Engdahl 1991; Engdahl *et al.* 1998). To properly account for the coupling of velocity and location, extensions likewise mostly rely on picking, but invert for the hypocentres and velocity structure simultaneously, which can lead to improved results (e.g. Aki & Lee 1976; Eberhart-Phillips 1986; Kissling 1988; Thurber 1992).

With the deployment of increasingly dense instrument arrays, wavefield-imaging techniques originally developed for controlled-source hydrocarbon exploration are starting to become powerful alternatives. Strongly related to the process of migration, it was shown that efficient localization can be achieved by backprojection (e.g. Ishii *et al.* 2005), reverse time modelling (Gajewski & Tessmer 2005), acoustic time reversal (Larmat *et al.* 2006) or diffraction stacking (e.g. Gajewski *et al.* 2007; Zhebel *et al.* 2011; Grigoli *et al.* 2013). Utilizing collective properties of the emerging wavefield, these methods can deal with high noise levels and the process of picking can be circumvented. Still, the respective results highly depend on the quality of the underlying velocity models and require sufficiently dense spatial wavefield sampling. Recently, the increasing capacity of computational resources has paved the way for combining these wavefield-based source imaging methods with the notion of joint location and velocity inversion. Wang & Alkhalifah (2018) have proposed a source function independent full waveform inversion (FWI) approach. In contrast to previous FWI-based methods (e.g. Sun *et al.* 2016) the need of a good starting guess of the velocity distribution has been relaxed by adopting a scheme which requires only a rough estimate of the vertical velocity variation. The method delivers accurate source locations and good velocity distributions. Nonetheless, the approach requires good data quality and generates high computational costs.

We propose an alternative, robust and efficient workflow to simultaneously estimate the velocity model and the source locations. The idea has initially been proposed by Schwarz *et al.* (2016) and exploits the fundamental robustness of coherence analysis. Stacking, forming a central ingredient of coherence analysis, has proven to be a reliable tool in controlled-source seismology and allows to access even weak events (e.g. Mayne 1962; Taner & Koehler 1969). Different traveltime operators have been proposed for coherence analysis over the years depending on different attributes (e.g. Landa *et al.* 2010; Schwarz *et al.* 2014). The common-reflection-surface method (Jäger *et al.* 2001) for instance delivers so-called wavefront attributes that describe the slopes and curvatures of the recorded wavefield. Apart from trace interpolation and data regularization (Baykulov & Gajewski 2009; Xie & Gajewski 2017) these attributes can be used for wavefront tomography (Duveneck 2004). The first step of our proposed method is to evaluate wavefront attributes for passive seismic data. Furthermore, we estimate the source excitation times of the recorded events by using an adapted traveltime operator. These source excitation times are then refined during wavefront tomography to eventually deliver a consistent velocity distribution. Finally, we use this velocity model for reverse time modelling to obtain an image function that localizes the recorded energy sources. Controlled synthetic and a challenging field data example suggest that the new approach is highly automatable and leads to reliable locations. Furthermore, the inversion delivers laterally resolved velocity structures even for severe noise contamination and data sparsity that is in strong violation of spatial wavefield sampling criteria.

2 WAVEFRONT ATTRIBUTES

The arrival time t of a passive seismic signal recorded at receiver location $\boldsymbol{x}$ can generally be expressed by

$$t(\boldsymbol{x}) = t_0(\boldsymbol{x}) + t_s \quad , \tag{1}$$

where t_0 is the actual traveltime from the source to the receiver and t_s marks the unknown source excitation time. In order to extract the event's kinematic information from the record, we want to use an analytic equation to approximatively represent the traveltime depending on the desired wavefront attributes. This can be achieved by means of a Taylor series expansion (e.g. Ursin 1982; Castle 1994). If we only consider receivers in the local vicinity of a given $\boldsymbol{x_0}$ according to

$$\boldsymbol{x} = \boldsymbol{x_0} + \boldsymbol{\Delta x} \quad , \quad \boldsymbol{x_0} = \begin{pmatrix} x_0 \\ y_0 \end{pmatrix} \quad , \quad \boldsymbol{\Delta x} = \begin{pmatrix} \Delta x \\ \Delta y \end{pmatrix} \quad , \tag{2}$$

where Δx and Δy are sufficiently small, the arrival time of the signal can be well approximated by the first-order Taylor series expansion about $\boldsymbol{x_0}$:

$$t(\boldsymbol{x}) \approx t(\boldsymbol{x_0}) + \boldsymbol{\nabla} t(\boldsymbol{x_0}) \cdot \boldsymbol{\Delta x} \tag{3}$$

$$\boldsymbol{\nabla} t = \left(\frac{\partial t}{\partial x} \; \frac{\partial t}{\partial y} \right) = \left(\frac{\partial t_0}{\partial x} \; \frac{\partial t_0}{\partial y} \right) \quad , \tag{4}$$

where $\boldsymbol{\nabla} t$ describes the gradient of t, which is similar to the gradient of t_0. Increasing the area of interest by regarding larger values of Δx and Δy, the second order term has to be taken into account:

$$t(\boldsymbol{x}) \approx t(\boldsymbol{x_0}) + \boldsymbol{\nabla} t(\boldsymbol{x_0}) \cdot \boldsymbol{\Delta x} + \frac{1}{2} \cdot \boldsymbol{\Delta x}^{\mathrm{T}} \cdot \underline{\mathbf{H}}(\boldsymbol{x_0}) \cdot \boldsymbol{\Delta x} \tag{5}$$

$$\underline{\mathbf{H}} = \begin{pmatrix} \frac{\partial^2 t}{\partial x^2} & \frac{\partial^2 t}{\partial x \partial y} \\ \frac{\partial^2 t}{\partial x \partial y} & \frac{\partial^2 t}{\partial y^2} \end{pmatrix} = \begin{pmatrix} \frac{\partial^2 t_0}{\partial x^2} & \frac{\partial^2 t_0}{\partial x \partial y} \\ \frac{\partial^2 t_0}{\partial x \partial y} & \frac{\partial^2 t_0}{\partial y^2} \end{pmatrix} \quad . \tag{6}$$

The 2×2 matrix $\underline{\mathbf{H}}$ corresponds to the Hessian. This parabolic traveltime expression contains five unknowns, that is the five derivatives. In fact, eq. (5) delivers a fairly good description of the moveout in the local vicinity of $\boldsymbol{x_0}$, however, the hyperbolic expression, obtained from eq. (5) by subtracting t_s, squaring both sides and ignoring terms of third and higher order in $\boldsymbol{\Delta x}$, is usually preferred in exploration seismology (e.g. Schleicher *et al.* 1993; Jäger *et al.*

Downloaded from https://academic.oup.com/gji/article-abstract/219/2/995/5539537 by Said Business School user on 23 September 2019

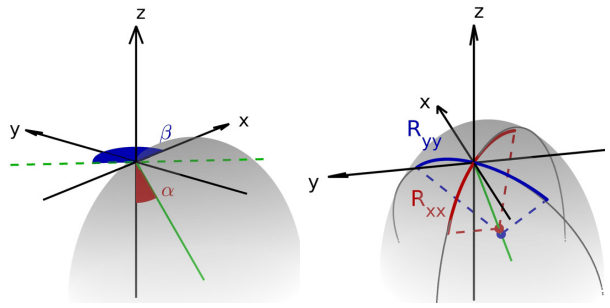


Figure 1. The transparent greyish surface marks a snapshot of an ellipsoidal wavefront in the instant of reaching the regarded receiver location, that is the centre of the coordinate system. The green line denotes the respective ray direction at the geophone. (left) Sketch of dip angle α and azimuth angle β in red and blue, respectively. The dotted line marks the projection of the ray direction onto the xy-plane. (right) The red and blue lines denote arcs with the radii R_{xx} and R_{yy}, respectively. The accordingly coloured dots mark the centres of the respective circles. The grey lines highlight the intersections of the $x'z'$-plane and $y'z'$-plane of the ray-centred coordinate system, in which the curvatures are evaluated, and the wavefront.

2001):

$$t(\boldsymbol{x}) \approx \Big[\big(t(\boldsymbol{x_0}) - t_s + \nabla t(\boldsymbol{x_0}) \cdot \boldsymbol{\Delta x}\big)^2 + \big(t(\boldsymbol{x_0}) - t_s\big) \cdot \boldsymbol{\Delta x}^{\mathrm{T}} \cdot \underline{\mathbf{H}}(\boldsymbol{x_0}) \cdot \boldsymbol{\Delta x}\Big]^{\frac{1}{2}} + t_s \quad . \tag{7}$$

As this formula additionally involves the source excitation time t_s, it contains six unknowns. In case of a homogeneous velocity model the expression is actually exact. Both eqs (5) and (7) deliver accurate fits and contain the physically interesting quantities ∇t and $\underline{\mathbf{H}}$. The gradient can be related to the horizontal slowness, composed of p_x and p_y, while the Hessian is linked to the curvature matrix $\underline{\mathbf{K}}$ (Hubral 1983):

$$\nabla t = \begin{pmatrix} p_x & p_y \end{pmatrix} = \begin{pmatrix} \dfrac{\sin(\alpha) \cdot \cos(\beta)}{v_0} & \dfrac{\sin(\alpha) \cdot \sin(\beta)}{v_0} \end{pmatrix} \tag{8}$$

$$\underline{\mathbf{H}} = \begin{pmatrix} H_{xx} & H_{xy} \\ H_{xy} & H_{yy} \end{pmatrix} = \frac{1}{v_0} \cdot \underline{\mathbf{L}} \cdot \underline{\mathbf{K}} \cdot \underline{\mathbf{L}}^{\mathrm{T}} \tag{9}$$

$$\underline{\mathbf{L}} = \begin{pmatrix} \cos(\alpha) \cdot \cos(\beta) & -\sin(\beta) \\ \cos(\alpha) \cdot \sin(\beta) & \cos(\beta) \end{pmatrix} \tag{10}$$

$$\underline{\mathbf{K}} = \begin{pmatrix} K_{xx} & K_{xy} \\ K_{xy} & K_{yy} \end{pmatrix} = \begin{pmatrix} 1/R_{xx} & 1/R_{xy} \\ 1/R_{xy} & 1/R_{yy} \end{pmatrix} \quad , \tag{11}$$

with α and β denoting the dip and azimuth angle, respectively, and v_0 indicating the locally, meaning within the regarded surrounding of $\boldsymbol{x_0}$, constant near-surface velocity. The rotation matrix $\underline{\mathbf{L}}$ accounts for a transformation from Cartesian to ray-centred coordinates. The wavefront curvatures K_{xx}, K_{xy} and K_{yy} are the reciprocals of the respective radii R_{xx}, R_{xy} and R_{yy}, all measured in ray-centred coordinates. Hence, there are five wavefront attributes: two angles and three curvatures. These attributes are visualized in Fig. 1, except for the mixed quantity R_{xy} which depends on the alignment of the ray-centred coordinate system with respect to the principal curvatures of the wavefront.

When considering only two dimensions, such that

$$\Delta y = 0 \quad , \quad \beta = 0 \quad , \tag{12}$$

eq. (5) simplifies to

$$t(x) \approx t(x_0) + \frac{\sin(\alpha)}{v_0} \cdot \Delta x + \frac{1}{2} \cdot \frac{\cos^2(\alpha)}{v_0 \cdot R_{xx}} \cdot \Delta x^2 \quad , \tag{13}$$

while eq. (7) becomes

$$t(x) \approx \left[\left(t(x_0) - t_s + \frac{\sin(\alpha)}{v_0} \cdot \Delta x\right)^2 + \big(t(x_0) - t_s\big) \cdot \frac{\cos^2(\alpha)}{v_0 \cdot R_{xx}} \cdot \Delta x^2\right]^{\frac{1}{2}} + t_s \quad . \tag{14}$$

The issue of estimating wavefront attributes for the recorded wavefield thus becomes an optimization problem, where the coherent energy locally stacked along an analytical traveltime curve has to be maximized for each sample. The measure used to quantify coherence in this work is the normalized semblance coefficient (Taner & Koehler 1969). As we have already pointed out, the parabolic eq. (5) is a function of only the five wavefront attributes, whereas the hyperbolic eq. (7) additionally depends on the unknown source excitation time t_s.

In a first step, we can therefore estimate the wavefront attributes of the data using eq. (5). Because these attributes are local quantities of the wavefield the optimization aperture used for this estimation should be as small as possible. This so-called optimization aperture corresponds to the maximum $|\boldsymbol{\Delta x}|$ considered for the fitting process. An alternative to optimizing the parabolic function for both first and second order attributes simultaneously is to find ∇t via eq. (3) first (Mann *et al.* 1999). However, this requires a dense receiver sampling and high signal-to-noise ratio (SNR). As by-product, the obtained wavefront attributes can be used to enhance the recorded data by creating a stack, summing up all the samples along the analytically defined traveltime trajectories within a certain range around $\boldsymbol{x_0}$.

Afterwards, we use the wavefront attributes determined in the previous step and maximize the semblance using eq. (7) to approximate t_s. Since the source excitation time is constant for each event, we use the entire data ($\Delta x \to \infty$ and $\Delta y \to \infty$) in this second optimization and compute the median of all estimates per event to obtain a final t_s value for each source. In this context, event tagging (e.g. Bauer *et al.* 2019b) is used to differentiate between signals from different sources. This automatic procedure evaluates the local similarity of wavefront attributes, counts the number of events in the data and assigns all samples baring high semblance values to their respective event number. Bauer *et al.* (2019b) have shown a successful application of tagging to active seismic field data containing various intersecting diffractions.

Since the moveout might become fairly complex and t_s is simply approximated from the best hyperbolic fit, the results may vary in quality. It appears, however, that especially for moderate velocity variations the approach generally delivers a good initial guess of the source excitation times (Schwarz *et al.* 2016). In order to refine this guess and eventually be able to spatially localize the sources with a consistent velocity model, we use wavefront tomography.

3 WAVEFRONT TOMOGRAPHY AND IMAGE FUNCTION

Following coherence analysis each sample can be associated with a maximum semblance value as well as a set of wavefront attributes, kinematically describing the dominant local wavefield. Furthermore, all tagged samples which are thus regarded as signal rather than noise can be related to an initial source excitation time.

Downloaded from https://academic.oup.com/gji/article-abstract/219/2/995/5539537 by Said Business School user on 23 September 2019

In order to get the input data $\boldsymbol{d}$ for wavefront tomography (Duveneck 2004; Bauer *et al.* 2017), the lateral coordinates $\boldsymbol{x}$, the traveltime $\tau = t - t_s$, that is the time t of the sample minus the corresponding estimate of the source excitation time, the horizontal slowness values $\boldsymbol{\nabla} t$ as well as the curvature related parameters $\underline{\mathbf{H}}$ and the event tag ξ are extracted automatically for samples exceeding a user-defined coherence threshold:

$$\boldsymbol{d}_i = (x, y, \tau, p_x, p_y, H_{xx}, H_{xy}, H_{yy}, \xi)_i \quad , \quad i = 1, \ldots, n_{\text{data}}, \tag{15}$$

with n_{data} denoting the total amount of picked data samples and $\boldsymbol{d}$ containing all $\boldsymbol{d}_i$.

The principal model components $\boldsymbol{m}$ on the other hand comprise the velocity model

$$v_{jkl}, \quad j = 1, \ldots, n_x, \quad k = 1, \ldots, n_y, \quad l = 1, \ldots, n_z, \tag{16}$$

defined in terms of B-splines (De Boor 1978), with n_x, n_y and n_z marking the number of nodes used in x-, y- and z-direction, respectively, and

$$(x_0, y_0, z_0, e_x, e_y)_i \quad , \tag{17}$$

where $(x_0, y_0, z_0)_i$ gives the starting location of the upwards propagating ray corresponding to the ith data subset $\boldsymbol{d}_i$ and the horizontal components $(e_x, e_y)_i$ of the unit vector $\hat{\boldsymbol{e}}_i$ determine the ray emittance direction at this subsurface point.

Provided that the source excitation time can be estimated correctly, τ equals the source–receiver traveltime t_0. However, τ might occasionally be biased by an erroneous source excitation time as the estimation of t_s via eq. (7) is approximative. Getting good approximations of t_s intrinsically requires knowledge of the velocity model. Thus, we refine t_s in the inversion by extending the model space to include the vector $\boldsymbol{t_r}$ that contains all

$$(t_r)_\xi \quad , \quad \xi = 1, \ldots, n_{\text{events}} \quad , \tag{18}$$

where t_r denotes the correction of the initial source excitation time and n_{events} is the number of detected events. Regarding a certain pick i, associated with tag ξ, the refinement shall obey:

$$t_i - (t_s)_\xi + (t_r)_\xi = \tau_i + (t_r)_\xi \stackrel{!}{=} (t_0)_i \quad . \tag{19}$$

Including this refinement in the inversion is supposed to link the information from multiple sources together. In order to obtain initial values for Expression 17, we assume an initial medium of constant near-surface velocity and set $\boldsymbol{t_r}$ equal to $\mathbf{0}$. Then, we use kinematic ray tracing to back propagate the picks $\boldsymbol{d}$ into the subsurface. This delivers the initial ray starting locations and directions. Afterwards, upward dynamic ray tracing is performed to obtain the modelled data $\boldsymbol{d}_{\text{mod}}$. This data set contains all $\boldsymbol{d}_i^{\text{mod}}$, the modelled counterparts of the surface location, the traveltime and the wavefront attributes in $\boldsymbol{d}_i$, which are generally given by

$$\boldsymbol{d}_i^{\text{mod}}(\boldsymbol{m}, \boldsymbol{t_r}) = \left(\boldsymbol{x}(\boldsymbol{m}), \tau(\boldsymbol{m}, \boldsymbol{t_r}), \boldsymbol{\nabla} t(\boldsymbol{m}), \underline{\mathbf{H}}(\boldsymbol{m})\right)_i^{mod} \quad , \tag{20}$$

where the traveltime $\tau_i^{mod} = (t_0^{mod})_i - (t_r)_\xi$, that is the modelled traveltime from the ray starting location to the surface minus the respective source excitation time refinement, analogous to eq. (19).

Accounting for errors in the attribute estimation, the inversion is implemented in a damped weighted least-squares sense (Tarantola 2005). The objective function reads

$$S(\boldsymbol{m}, \boldsymbol{t_r}) = \tfrac{1}{2} \left\| \left(\boldsymbol{d} - \boldsymbol{d}_{\text{mod}}(\boldsymbol{m}, \boldsymbol{t_r})\right) \cdot \boldsymbol{W} \right\|_2^2 + \Lambda(v_{jkl}) \quad , \tag{21}$$

with $\boldsymbol{W}$ denoting the weighting vector that scales the different physical quantities and $\Lambda(v_{jkl})$ representing the regularization term, favouring smooth velocity models. When evaluating the difference of $\boldsymbol{d}$ and $\boldsymbol{d}_{\text{mod}}$ the event tag is ignored. Note, however, that not only the wavefront attributes, but also the surface location $\boldsymbol{x}$ and the traveltime τ are fitted in the inversion.

Following a fairly pragmatic approach, we decouple the principal model space $\boldsymbol{m}$ and the source excitation time refinements $\boldsymbol{t_r}$ and simply minimize S as a function of the source excitation time refinements, where the number of unknowns equals the number of tagged events. In each iteration of this optimization a certain constellation of source excitation time refinements is fixed. The objective function is then minimized depending on $\boldsymbol{m}$ only. The modelling operator used to compute $\boldsymbol{d}_{\text{mod}}(\boldsymbol{m})$ for a given $\boldsymbol{t_r}$ is linearized locally by means of Fréchet derivatives, which are computed via ray perturbation theory (Farra & Madariaga 1987; Duveneck 2004). Thus, the objective function $S(\boldsymbol{m})$ can be minimized iteratively using the LSQR algorithm (Paige & Saunders 1982). The final objective function value is then assigned to the tested set of source excitation time refinements. The minimum $S(\boldsymbol{t_r})$ value is obtained using a pattern search algorithm (Hooke & Jeeves 1961). More sophisticated algorithms might be exploited in future applications, however, the pattern search algorithm has provided reliable results and performance. In fact, the number of unknowns, being the number of events in the data, is usually fairly small and allows for various simple optimization algorithms.

This finally delivers a velocity model along with the corresponding ray starting points that is consistent with the input data $\boldsymbol{d}$. Furthermore, if enough sources from a similar area contribute to the process, it leads to an effective refinement of the involved traveltimes.

As the initial ray starting locations are governed by kinematic ray tracing, they depend on $\boldsymbol{x}$, τ and $\boldsymbol{\nabla} t$. Thus, the first update of each minimization of $S(\boldsymbol{m})$ only depends on the difference of the measured and modelled second order attributes. As the quality of the wavefront attributes usually decreases with increasing order, that is angles are more reliable than curvatures, this might be undesirable. Recent developments have overcome this problem by applying focussing constraints (Bauer *et al.* 2019a). Alternatively, one can adjust $\boldsymbol{W}$ in the objective function to give more weight to the angles than to the curvatures. While in active seismic, one would obviously like to attach most weight to the traveltimes, representing zero order attributes, angles appear to be the most reliable quantities in the passive seismic scenario.

The final velocity model can be used for reverse time modelling (Gajewski & Tessmer 2005). In the given examples we utilize the acoustic wave equation for constant density:

$$\nabla^2 \psi = \frac{1}{V^2} \cdot \frac{\partial^2 \psi}{\partial t^2} \quad , \tag{22}$$

where $\psi = \psi(x, y, z, t)$ is the pressure field and $V = V(x, y, z)$ denotes the acoustic velocity. Considering the time-reversed seismic data as surface boundary values, we model the wave propagation by finite differences until a predefined maximum time T is reached. The image function $f = f(x, y, z)$ resembles an energy and is given by

$$f = \int_0^T \psi^2 \, \mathrm{d}t \quad . \tag{23}$$

The image function finally allows for a spatial, quasi-probabilistic localization of the source energy by using the entire recorded wavefield depending only on the recovered velocity distribution, but not on the estimated source excitation times. The velocity model might of course be biased by inaccurate traveltimes implicitly, but the

Downloaded from https://academic.oup.com/gji/article-abstract/219/2/995/5539537 by Said Business School user on 23 September 2019

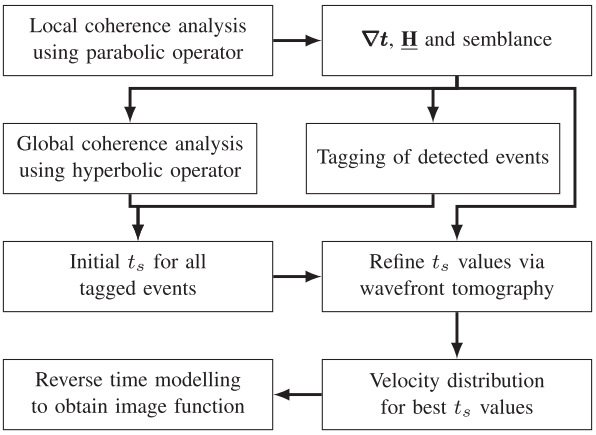


Figure 2. Flowchart of our proposed workflow, sketching the main algorithms and their respective outcomes.

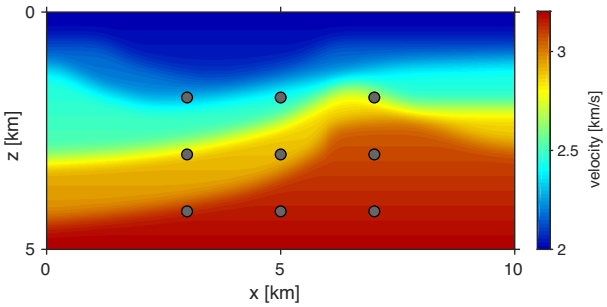


Figure 3. Velocity model and event locations (grey dots) for the synthetic data examples.

source locations, previously represented by the ray starting locations in the tomography, now follow without an explicit definition of the source excitation times. This does not mean that all traveltime errors vanish, however, they can be significantly reduced.

The overall workflow, starting from determining the wavefront attributes to eventually obtaining a consistent velocity distribution as well as source locations in space, is sketched in Fig. 2.

4 NUMERICAL EXAMPLES

To test our proposed approach we first consider the optimal case of a densely sampled acquisition recording high-amplitude events. In order to show the benefits and underline the robustness of the method we subsequently show results for noise-contaminated and sparse data. For all three synthetic data examples we utilize the same velocity model and nine explosive sources, see Fig. 3. The events are shifted by arbitrary source excitation times ranging from −1.50 to 6.55 s. The data sets are simulated via finite-difference modelling, the recording time measures 10 s and the time sampling is 4 ms. The dominant frequency of the signals is about 10 Hz. Such a low frequency, however, is only chosen for visualization purposes but not relevant for the success of the approach. Similarly, the workflow can be applied to all scales of events. Hence, it can equally deal with source depths of tens or even hundreds of kilometres if the acquisition surface is accordingly stretched.

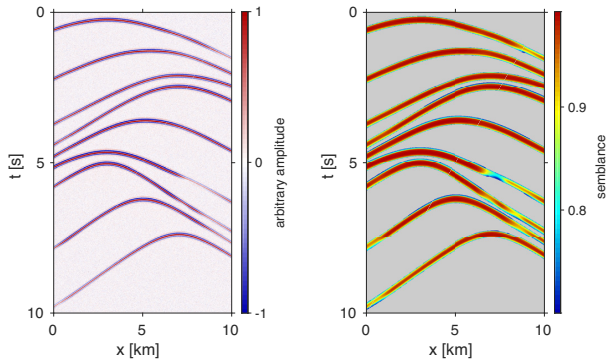


Figure 4. Left-hand panel: seismic surface recording for the first experiment. The colourbar is clipped at a half of the overall maximum amplitude. Right-hand panel: maximum semblance values obtained via the parabolic traveltime operator. Samples with a semblance value smaller than 0.7 are masked grey.

4.1 Proof of concept

For the first example we consider a total of 501 receivers which are equally distributed along the surface of the model in Fig. 3, thus the receiver distance measures 20 m. We add Gaussian noise with a SNR of 20. The resulting seismic data are illustrated in Fig. 4(left-hand panel).

Following our proposed workflow, we start by performing a local coherence analysis with the parabolic traveltime operator, eq. (5), to obtain wavefront attributes for the recorded wavefield. In this example, we use an optimization aperture of 700 m. The coherence section, denoting the maximum semblance value for each sample, is shown in Fig. 4(right-hand panel). The semblance values are apparently high along the nine events but low elsewhere. The resulting α and R_{xx} values are displayed in Fig. 5(top panel) and reveal smooth and physically reasonable variations.

As a next step, we fix these attributes and search for the optimal hyperbolic fit, eq. (7), for each sample of the data. Thereby, we obtain t_s as displayed in Fig. 5(bottom left-hand panel). From a physical point of view, the source excitation time should be constant for each event. Since it is calculated using an analytical fitting operator, it seems obvious though that there might be variations along the events when laterally heterogeneous media are considered. While one can still assign a dominant colour and consequently a dominant source excitation time to each event, these t_s values may not necessarily be good approximations. In order to further investigate the quality of the estimated source excitation times, we tag the nine events. As there are no intersecting events in our example, this can simply be done by automatically labelling connected structures when ignoring samples with low coherence in the semblance section, compare Fig. 4(right-hand panel). The tagging result is displayed in Fig. 5(bottom right-hand panel). Thereby, we can assign the estimated source excitation times to the different events, analyse the arising deviations per source and compute median values to obtain a single t_s value for each tag. In Fig. 6 we compare these results with the actual source excitation times. When considering the event-wise median values (dotted lines), the t_s approximations are in fact quite good in six of the overall nine cases. The three erroneous source excitation times, however, differ from the true values by up to 0.9 s. This illustrates how using global traveltime fits, that is trying to describe the entire wavefront with one analytic expression, to estimate source excitation times in laterally heterogeneous media may be insufficient for some events. First and foremost, the order

Downloaded from https://academic.oup.com/gji/article-abstract/219/2/995/5539537 by Said Business School user on 23 September 2019

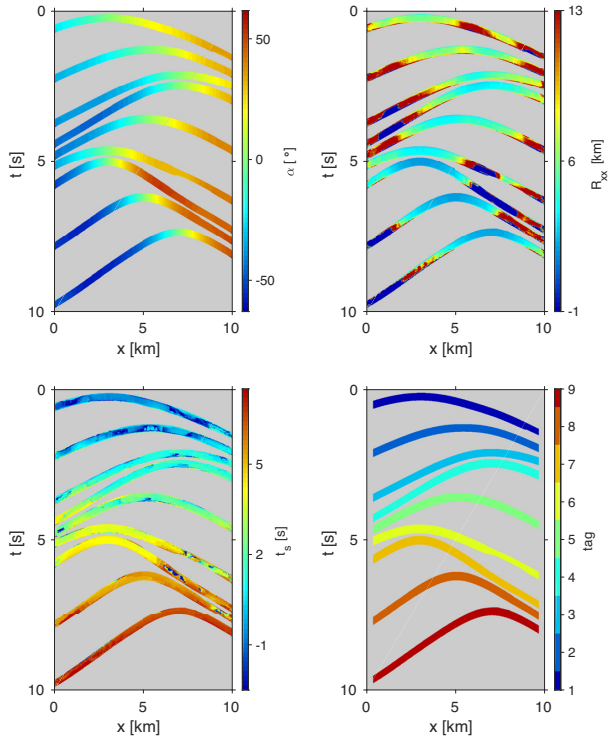


Figure 5. Visualization of wavefront attributes α (top left-hand panel:) and R_{xx} (top right) as well as sample-wise source excitation times t_s (bottom left). Contributions from samples with low coherence are masked grey. The R_{xx} values are clipped at −1km and 13km, respectively. (bottom right) Tagging result. The boundaries of the acquisition are muted prior to the labelling procedure to account for possible boundary effects in the coherence estimation.

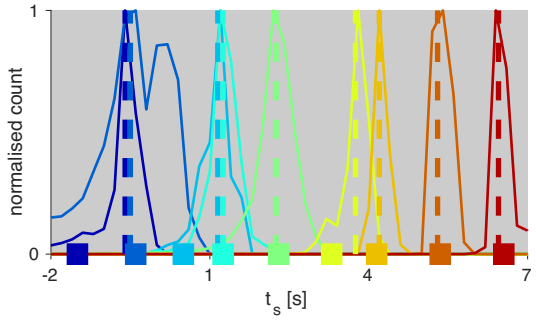


Figure 6. The nine colours match the tag numbers in Fig. 5(bottom right-hand panel:). The centres of the squares at the bottom of the plot mark the actual source excitation times. The continuous lines sketch the normalized counts of all estimated t_s values per event and therefore resemble histograms. Contributions from samples that are assigned low coherence during the hyperbolic fitting process are ignored. The dashed lines denote the resulting median values.

of the respective error is linked to the order of lateral heterogeneity the signal undergoes on its way to the surface. Overall, this leads to significantly biased input data for wavefront tomography.

Therefore, we need to refine the source excitation times. The tag-wise median values of the previously estimated source excitation times constitute our initial guess for wavefront tomography. As previously explained, the space of unknowns is split into the source excitation time refinements $\boldsymbol{t_r}$ and the principal model space $\boldsymbol{m}$. The minimum $S(\boldsymbol{t_r})$ value eventually delivers refined t_s values for

Table 1. List of the true source excitation times t_s^{true}, the via parabolic fitting estimated values t_s^{ini} and the refined times t_s^{ref}, where $t_s^{\text{ref}} = t_s^{\text{ini}} - t_r$, for each tagged source.

Tag	t_s^{true} [s]	t_s^{ini} [s]	t_s^{ref} [s]
1	−1.50	−0.60	−1.73
2	−0.40	−0.50	−0.58
3	0.50	1.15	0.36
4	1.25	1.25	1.09
5	2.30	2.25	2.14
6	3.30	3.75	3.15
7	4.15	4.20	4.08
8	5.35	5.30	5.26
9	6.55	6.45	6.46

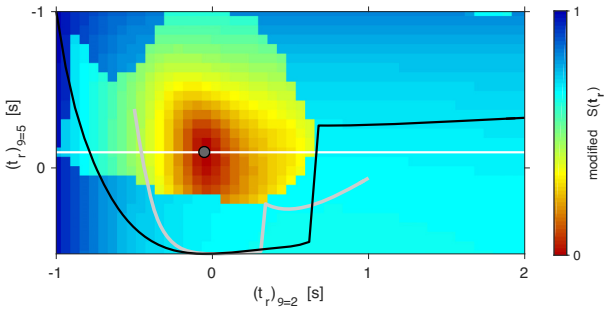


Figure 7. Visualization of the modified objective function $S(\boldsymbol{t_r})$ when using the exact source excitation time t_s^{true} for each tag except 2 and 5. The modified objective function value follows from min–max normalization of the natural logarithm of $S(\boldsymbol{t_r})$. The grey dot marks the position of the true value. The black line sketches the shape of the actual objective function, that is without logarithm, for the profile denoted by the white line. The light grey line sketches the objective function obtained when using t_s^{true} for all nine events but adding the same refinement between −0.5 and 1 s to all of them. It is scaled like the black curve.

the nine events. In Table 1 we compare the true, initial and refined source excitation times. We observe that the large errors of events 1, 3 and 6 are reduced significantly and all nine source excitation times are sufficiently well approximated. However, all refined source excitation times are underestimating their true values by about 0.1–0.2 s. This might for instance be due to the optimization algorithm, the node spacing, the regularization and weighting factors or the initial velocity distribution and will be subject to further investigation in the future.

Fig. 7 visualizes the objective function when searching for only two source excitation time refinements, that is for events 2 and 5, while fixing the true values for the other seven events. In fact, the objective function shows a smeared minimum around the location of the actually necessary source excitation time refinements. The discontinuities of the objective function, see abrupt changes in colour, separate areas where the inversion has converged, i.e. lower objective function values, from areas where it has been unstable, that is higher objective function values taken from initial iterations. This area is controlled by the choice of regularization and weighting factors. Overall, the objective function is fairly flat in the vicinity of its minimum. This is also illustrated by the black curve in Fig. 7 that shows a single profile line of the surface. The relatively small gradient near the minimum illustrates the hypocentre-velocity coupling, as wrong velocities, inducing wrong source excitation times and consequently wrong source locations, still allow for a fairly good fit of the data. Obviously, this illustration is insufficient for examining the entire behaviour of the optimization problem. As we

Downloaded from https://academic.oup.com/gji/article-abstract/219/2/995/5539537 by Said Business School user on 23 September 2019

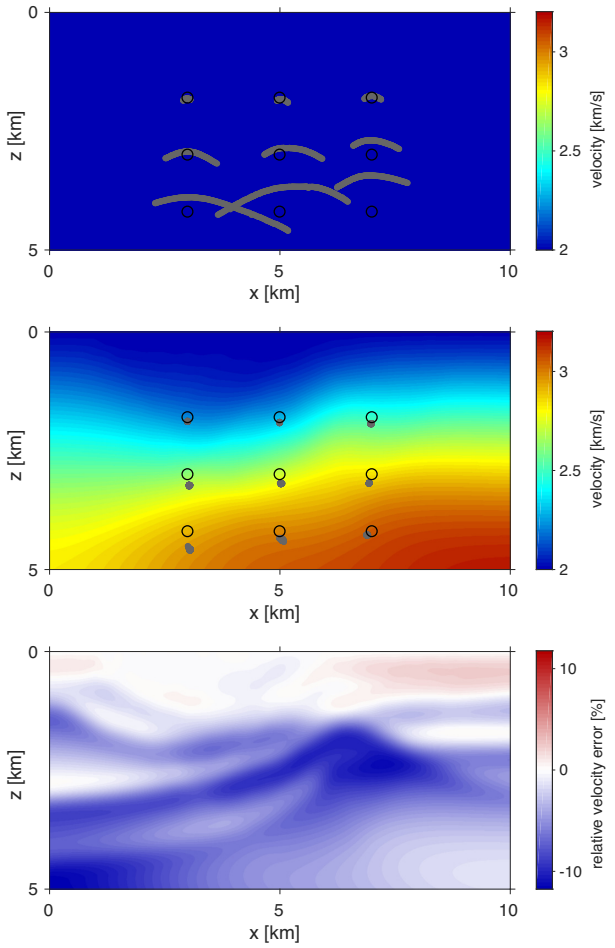


Figure 8. Top panel: initial model. Middle panel: final model. The grey dots mark the ray starting locations for the respective velocity models, the black circles show the actual source positions. The colourbars are clipped at the minimum and maximum velocity values of the true model. Bottom panel: relative velocity error.

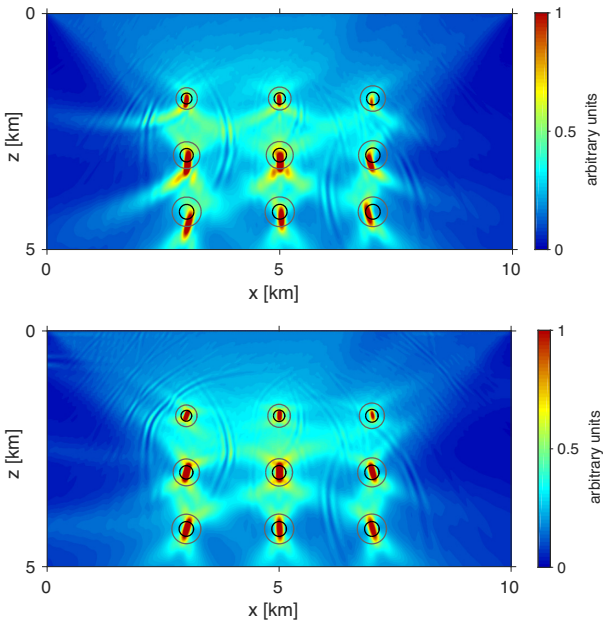


Figure 9. Image functions. The colourbars are clipped at 40 per cent of the respective maximum energies. The circles are centred at the true source locations. Black circles have a radius of half, grey circles of once the dominant signal wavelength. Top panel: image function obtained from reverse time modelling for the estimated velocity distribution in Fig. 8(middle panel). Bottom panel: image function obtained from reverse time modelling for the true velocity model.

seek to refine all nine source excitation times simultaneously, the properties of the objective function appear more complex. The light grey line in Fig. 7 sketches the objective function when using the exact source excitation times for all nine events but adding the same variable time shift to all of them. Thus, only the source excitation time differences between the events are correct while the absolute values for all sources are equally shifted. Again, this leads to a very flat objective function in the vicinity of the true value, suggesting that as long as the source excitation time differences are estimated correctly the velocity model can be scaled accordingly to deliver a good data fit. Nonetheless, the absolute minima of both curves in Fig. 7 are at the expected locations.

Finally, we can also examine the respective velocity distribution and ray starting locations. Using the refined source excitation times the initial guess of the parameters $\boldsymbol{m}$ is illustrated in Fig. 8(top panel). The velocity distribution is homogeneous with value v_0 and the corresponding ray starting locations follow from downward kinematic ray tracing. The final model is displayed in Fig. 8(middle panel). One can easily recognize some of the underlying velocity features, as for instance the low-velocity moat in the shallower left part and the deeper rightwards rising high-velocity layer. Additionally, the final ray starting points clearly cluster in nine distinct regions close to the true source locations. These clusters, however, are all slightly too deep. This is a result of the generally underestimated source excitation times. When evaluating the relative velocity error, Fig. 8(bottom panel), we denote a maximum absolute value of nearly 12 per cent. This error is due to the underestimation of the velocities in particular at the top of the fast layers. The general underestimation of velocities is probably also a result of the underestimated source excitation times. Still, the long-wavelength velocity structure is resolved quite successfully. Obviously, only those regions of the model that have been traversed by rays contain reliable velocity information. In this sense, the bottom left and bottom right part of the model result from the regularization.

Finally, we can use the recovered velocities to perform reverse time modelling. In so doing we localize the energy sources of the recorded wavefield in a more probabilistic and continuous manner. The resulting image function can be seen in Fig. 9(top panel). It reveals nine distinct regions of relatively high energy that nicely coincide with the actual source locations, generally deviating by less than the dominant wavelength of the signals. The source depths, however, tend to be slightly overestimated. This is again linked to the underestimated velocities. The image function shows a much better resolution in lateral direction than in depth, that is the red maxima are smeared vertically. This is a consequence of having a laterally limited acquisition with receivers only at the surface. As the velocity model is of course erroneous itself, the image function does not illustrate the entire localization uncertainty. Fig. 9(bottom panel) shows the image function for the true velocity model. In fact, it shows an improved localization and energy-focussing, however, our method delivers comparable results without needing an accurate *a priori* velocity model.

All in all, these results confirm the functionality of our proposed method. Assuming knowledge of only the locally constant near-surface velocity, we are able to approximate the coarse velocity

Downloaded from https://academic.oup.com/gji/article-abstract/219/2/995/5539537 by Said Business School user on 23 September 2019

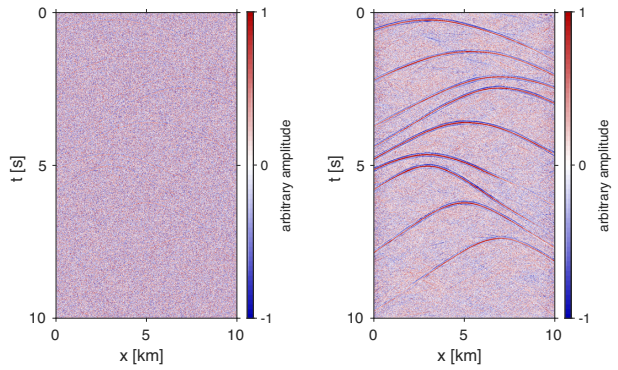


Figure 10. Left-hand panel: seismic surface data with an SNR of 0.5. Right-hand panel: enhanced data set, obtained from stacking according to the estimated wavefront attributes α and R_{xx}. The stacking aperture measures 700 m, hence 71 receivers contribute to each stacked trace. Both colourbars are clipped at a half of the respective overall maximum amplitude.

distribution and localize the sources in the subsurface. Note, that the near-surface velocity is only used for creating the initial velocity model but not inherently necessary for the approach, as the inversion is with respect to the derivatives ∇t and $\underline{\mathbf{H}}$ and not their physical interpretation as angles and curvatures. The only requirement is that the wavefronts of the signals are smooth within the local optimization apertures used to determine the wavefront attributes. As the initial guess of the source excitation times is taking into account very large optimization apertures, its quality is easily affected by strong lateral heterogeneity. To some extent, this can be accounted for by refining the traveltimes during inversion. The following examples further examine the method by considering the influences of noise and sparse spatial sampling.

4.2 Noisy data

The data set for this example equals the previous one except for the SNR which is set to 0.5. The corresponding data are displayed in Fig. 10(left-hand panel). Due to the high noise level and low signal amplitudes, respectively, the nine events are poorly visible.

Because of the intrinsic robustness of coherence analysis we can still estimate wavefront attributes for the data. In order to reach significant coherence levels that allow to distinguish signal from noise, the optimization aperture has to be sufficiently wide. We choose an optimization aperture of 1000 m for the hyperbolic traveltime fitting. As already mentioned, the wavefront attributes do not only enable wavefront tomography, but also allow for data enhancement by stacking. This can be comprehended in Fig. 10(right-hand panel). The previously invisible events are now fairly distinct. The signal only remains noisy in areas of particularly low amplitudes, straight slopes and in the vicinity of the acquisition boundaries, hence, wherever the attribute estimation is particularly difficult.

Estimating t_s values and tagging the events allows for evaluating a median source excitation time for each tagged source. Refining these times during the inversion leads to the final model parameters in Fig. 11(top panel). Again, having started from a constant near-surface velocity medium, the final velocity distribution maps the main features of the model, although it might seem less accurate in some areas compared to Fig. 8(middle panel). Furthermore, the focussing of the ray starting locations appears slightly worse and reveals distinct offsets compared to the true source locations, especially for the two events localized at the bottom left and bottom right

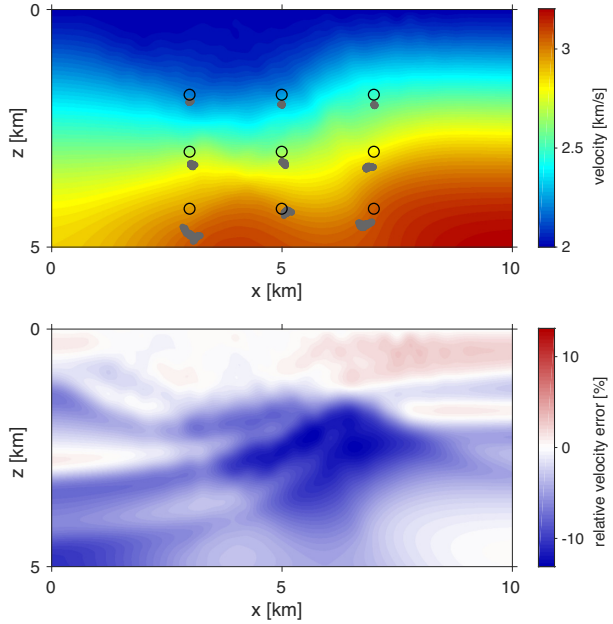


Figure 11. Top panel: final tomographic velocity model for the noisy data set. The grey dots mark the final ray starting locations, the black circles show the actual source positions. The colourbar is clipped at the minimum and maximum velocity values of the true model. Bottom panel: relative velocity error.

of the model. These larger errors are induced by the wavefront attributes which are slightly less accurate due to the high noise level. The relative error of the velocities is shown in Fig. 11(bottom panel). The erroneous underestimated area in the centre seems to be slightly extended in space. The maximum absolute value of the relative error measures more than 13 per cent and is thus marginally higher than in the previous experiment. Altogether, the overburden structure is in fact similarly resolved—despite the poor data quality.

Fig. 12(top panel) shows the image function when using the enhanced data set and the estimated velocities. Due to the still relatively high noise level in the stack, the background noise of the image function is high. Note, however, that without the enhanced data set the image function would show noise only and could not be used at all. This is illustrated in Fig. 12(bottom panel), where we have used the true velocity model and the unprocessed seismic data. Most of the energy in the image, that is Fig. 12(top panel), gets focussed in nine distinct regions, generally close to the true source locations. As a matter of fact, these peaks seem to be located slightly better than the final ray starting locations in Fig. 11(top panel). This is, as previously pointed out, due to the fact that for the ray tracing both the erroneous velocities and the erroneous traveltimes are implicated, while for the reverse time modelling only the velocities matter. Only the leftmost event exhibits a slightly larger error in the image function, however, it is still within once the dominant wavelength.

Considering that we have started with the data in Fig. 10(left-hand panel) and exploited no detailed *a priori* information, these results are surprisingly good. However, such noisy acquisition environments implicate a trade-off between increasing the optimization aperture to detect signals during the coherence analysis and keeping it small to enable a local wavefront attribute estimation and thus obtain high quality input data for the inversion. The suggested approach is generally applicable independent of high noise levels and

Downloaded from https://academic.oup.com/gji/article-abstract/219/2/995/5539537 by Said Business School user on 23 September 2019

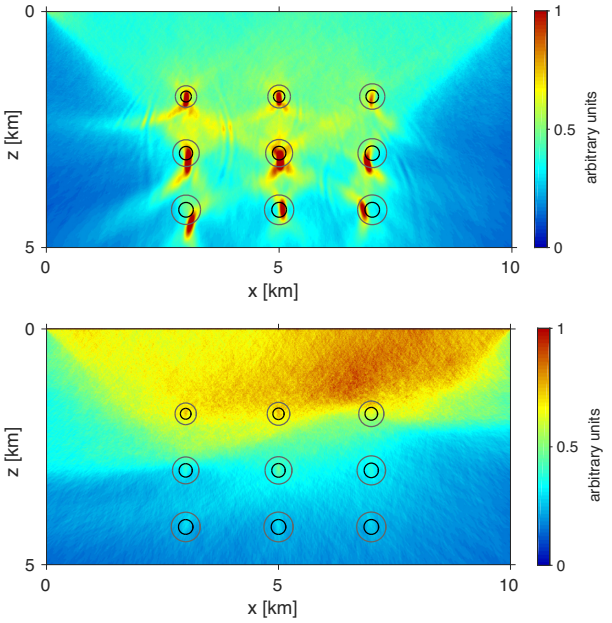


Figure 12. Image functions. The colourbars are clipped at 21 per cent of the respective maximum energies. The circles are centred at the true source locations. Black circles have a radius of half, grey circles of once the dominant signal wavelength. Top panel: image function obtained from reverse time modelling for the estimated velocities and the enhanced data, Fig. 10(right-hand panel). Bottom-hand panel: image function obtained from the unprocessed data, Fig. 10(left-hand panel), and the true velocity model.

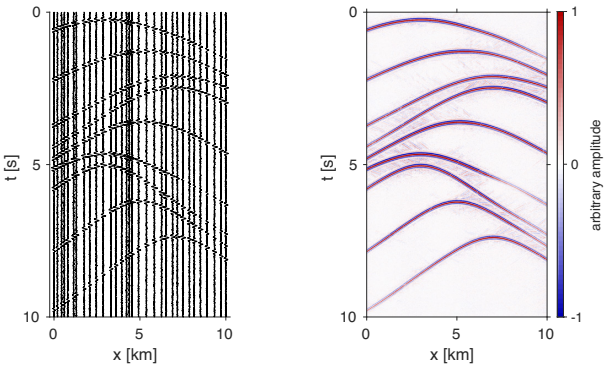


Figure 13. Left-hand panel: seismogram using a random selection of only 32 stations. Right-hand panel: enhanced and regularized data, obtained from stacking according to the estimated wavefront attributes α and R_{xx}. The stacking aperture measures 700 m. In order to reduce spatial aliasing artefacts the stack has been weighted with the smoothed semblance section. The colourbar is clipped at a half of the overall maximum amplitude.

low signal amplitudes, respectively, but might decrease in quality with decreasing SNR.

4.3 Sparse data

Finally, we want to analyse the influence of sparse data sampling. Therefore, we use a random selection of 32 from the previously used 501 receivers. The geophone distances vary from 160 to 460 m. We add Gaussian noise with a SNR of 10. The seismic data are visualized in Fig. 13(left-hand panel).

As a matter of fact, the estimation of wavefront attributes not only allows for increasing the SNR, it also enables data interpolation.

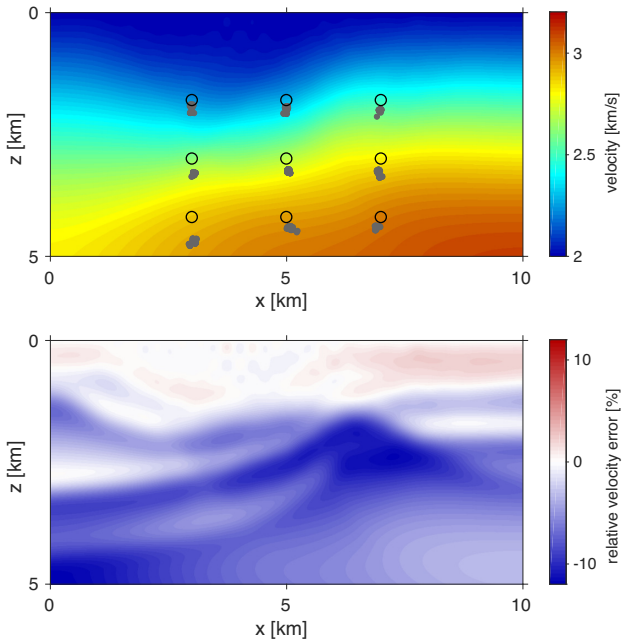


Figure 14. Top panel: final tomographic model. The grey dots mark the ray starting locations, the black circles show the actual source positions. The colourbar is clipped at the minimum and maximum velocity values of the true model. Bottom panel: relative velocity error.

This can easily be achieved by estimating the wavefront attributes for all lateral positions that one wants to interpolate the data at. Having those attributes, one can simply create a stack to locally interpolate the recorded wavefield. We use an optimization aperture of 1000 m to estimate α and R_{xx} and create an interpolated stack, see Fig. 13(right-hand panel). While the stacked seismogram reveals some minor artefacts due to spatial aliasing (compare the high-amplitude slanting stripes especially at the left-hand side at about 5 s), the events are still nicely interpolated. After all, such aliasing can easily be further suppressed, for instance by a more constrained attribute estimation. Considering the reverse time modelling this denser data should allow for a smoother image function displaying less imaging artefacts than the original data.

As before, the source excitation times are estimated and tag-wise refined to eventually deliver a consistent inversion result starting again from a constant near-surface velocity medium. The final velocity distribution is shown in Fig. 14(top panel). The recovered velocities are quite similar to the two previous results, while the focussing of the ray starting locations is marginally better than for the noisy data set. However, the positions of the nine clustering regions are again slightly too deep, in particular considering the deepest, leftmost event. The relative velocity error, Fig. 14(bottom panel), is similar in shape and magnitude to the one for the first data set. Thus, the maximum absolute value measures approximately 12 per cent, but the absolute values on average range from 4 to 5 per cent.

Finally, we use the interpolated seismic section, Fig. 13(right-hand panel), along with the estimated velocity distribution and perform reverse time modelling. In fact, the image function, Fig. 15(top panel), looks very similar to the one in Fig. 9. Compared to the image obtained from the true velocity model and the unprocessed seismic data [see Fig. 15(bottom panel)], the workflow-intrinsic data interpolation reduces the aliasing artefacts considerably. Especially the three shallow events appear more pronounced when using the improved data set. In general, the nine energy peaks in

Downloaded from https://academic.oup.com/gji/article-abstract/219/2/995/5539537 by Said Business School user on 23 September 2019

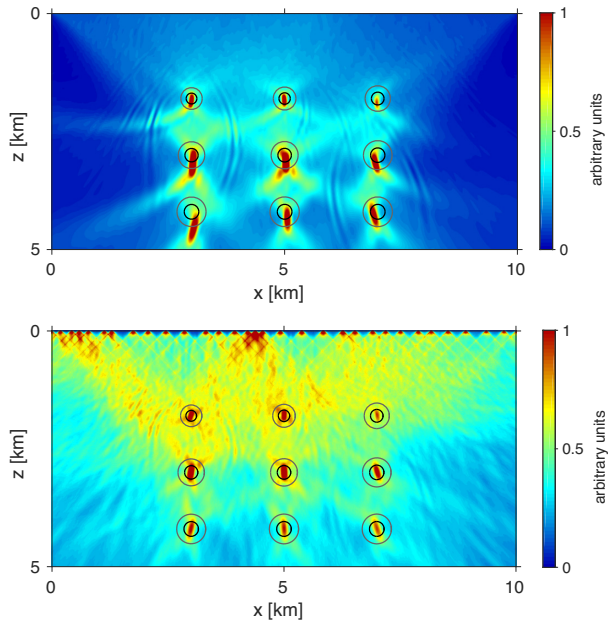


Figure 15. Image functions. The colourbars are clipped at 40 per cent of the respective maximum energies. The circles are centred at the true source locations. Black circles have a radius of half, grey circles of once the dominant signal wavelength. Top panel: image function obtained from reverse time modelling for the enhanced and regularized data, Fig. 13(right-hand panel), and the estimated velocities. Bottom panel: image function for the unprocessed data, Fig. 13(left-hand panel), and the true velocity model.

Fig. 15(top panel) coincide nicely with the true source locations. Some of the maxima, however, appear to some extend blurred and slightly mislocated, but overall the method delivers good results.

Even from such a sparse acquisition with only 32 stations along a 10 km profile we can still get a sufficiently accurate approximation of the velocity model and thereby localize the sources via reverse time modelling. We do not need detailed *a priori* information and perform data interpolation on the fly. Sparser sampling or larger data gaps would require a larger optimization aperture and thereby decrease the quality of the wavefront attributes. Nonetheless, the workflow can generally deal with sparse acquisitions.

5 FIELD DATA EXAMPLE

In order to check the performance of our approach in a realistic 3-D setting, we use seismic field data from an earthquake in northern Argentina. It took place in September 2008 with a moment magnitude of 6.3, originating from the area of the subducting Nazca Plate (Anderson *et al.* 2007). We utilize data that has been recorded by two local seismological arrays on the border between Argentina and Chile (Sandvol & Brown 2007; Beck & Zandt 2007). According to the officially estimated hypocentre (International Seismological Centre 2015), the source depth measures about 571 km. We have used a total of 76 receivers and roughly processed the data by means of resampling, mean subtraction and trace wise normalization. Furthermore, we have low-pass filtered the data with a cut-off frequency of 0.4 Hz in order to get smoother waveforms for the coherence analysis. We concentrate on the area of the first arrival for further investigations. The final seismic data is illustrated as a function of the expected epicentral distance (International Seismological Centre 2015) in Fig. 16. Fig. 17(left-hand panel) sketches the receiver locations and the expected epicentre. This setting is far

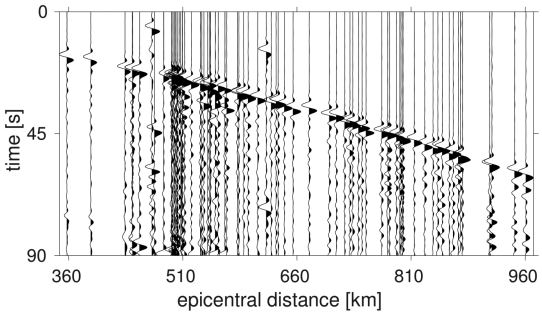


Figure 16. Seismic field data showing a deep earthquake. In order to visualize the moveout of the event, we have sorted the traces according to the distance from the expected epicentre.

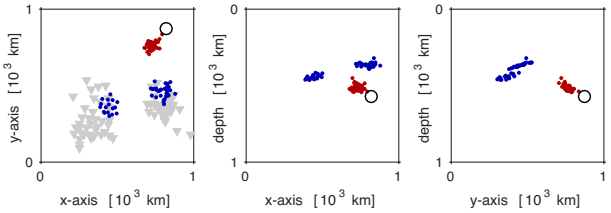


Figure 17. Seismic receivers are denoted by grey triangles. The black circle marks the expected hypocentre. The initial ray starting locations are illustrated in blue, the final points in red. The plots show views from the top(left-hand panel), and the two sides (middle, right-hand panels).

from perfect, as the epicentre lies beyond the acquisition surface and the amount of accessible data is small.

First, we need to determine wavefront attributes. As the data is very sparse and there are five unknown wavefront attributes in 3-D, we have chosen the optimization aperture to always contain all 76 traces. This allows for a relatively stable coherence analysis but smooths lateral variations. The source excitation time, estimated using the hyperbolic traveltime operator and averaged over all tagged samples, is only about 2 s off compared to the expected value (International Seismological Centre 2015).

As the data set only contains a single event, we have not refined the source excitation time in the inversion. This refinement approach is generally supposed to be most helpful, when there are multiple events in a similar area, as it links their source excitation times to each other rather then estimating them separately. Thus, we set t_r to zero and only invert for $\boldsymbol{m}$ in this example.

The initial velocity model is homogeneous. We set this initial velocity to 4468 m s^{-1}, which is inspired by the *P*-wave velocities of the 1-D anisotropic preliminary reference earth model (Dziewonski & Anderson 1981) and about an averaged value for the first 25 km depth, that is the order of the vertical node spacing in the tomography. The initial ray starting locations, that is the back propagated data picks for the constant velocity medium, along with the final locations are displayed in Fig. 17. While the picks are scattered and unfocussed in the initial model, they appear clearly focussed in the final velocity medium. Furthermore, the region where the points cluster is relatively close to the expected hypocentre. The estimated velocity model is shown in Fig. 18. In order to analyse its quality, we compare its averaged 1-D structure with the preliminary reference Earth model (PREM). The inversion fails to resolve single layers accurately, however, it reaches similar velocities in the depth of the earthquake. As we have used only a single source to create this model, the relatively poor resolution is not surprising. Furthermore, we have set the initial velocity to match the velocities in the

Downloaded from https://academic.oup.com/gji/article-abstract/219/2/995/5539537 by Said Business School user on 23 September 2019

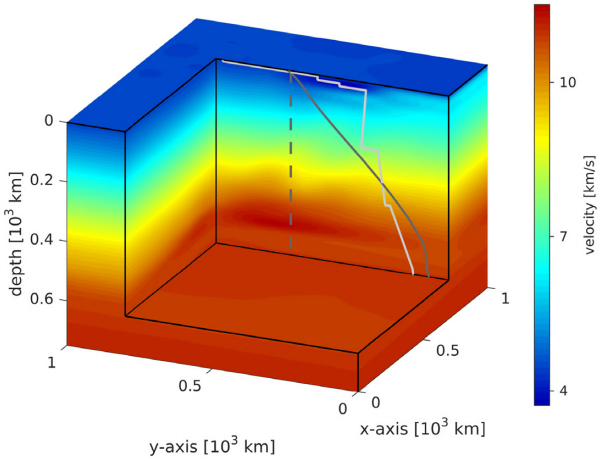


Figure 18. Illustration of the estimated 3-D velocity model. The three lines sketch the constant initial velocity (dashed dark grey), the lateral mean of the estimated velocities (dark grey) and the vertical *P*-wave velocity according to the preliminary reference earth model (light grey), all equally scaled.

area of the upper most nodes only. Thus, the value is very far from the high velocities in only slightly deeper layers. Still, the retrieved velocities reveal a reasonable trend and allow for a plausible localization. This underlines the general robustness of the workflow. In order to improve the approximated hypocentre and estimate its resolution induced localization uncertainty one could apply reverse time modelling.

Earthquakes are commonly located using data from various seismological arrays, providing good data coverage, and relying on a given velocity model. We have used seismic *P*-wave data from only two local arrays, to localize a single deep earthquake without needing a velocity model. The presented solution simplifies the physical processes immensely, for instance by ignoring the source mechanism and anisotropy, but still localizes the earthquake in the area of the expected hypocentre.

6 DISCUSSION

Using wavefront attributes of passive seismic data we have presented a workflow for simultaneous localization and velocity model building. The method needs basically no *a priori* information. However, we have assumed to know the near-surface velocity for the presented examples. In general, even a rough estimate of the average velocity of the upper layers should constitute an adequate starting guess for the inversion. The wavefront attribute estimation and the inversion are carried out in an automatic manner, where the optimization apertures in the coherence analysis and the regularization and weighting factors as well as the node spacing in the tomography have to be adjusted empirically. No time-consuming user interaction, as for instance manual picking, is required.

In order to use the method successfully, the quality of the estimated wavefront attributes is crucial. Ideally, the apex areas of the events of interest are covered by a dense acquisition to enable a reliable, local attribute estimation, particularly considering wavefront curvatures. The denser the areas are sampled, the smaller the necessary optimization apertures and thus the better the quality of the wavefront attributes. As apex area we refer to a circular surface with a radius of roughly the source depth centred at the epicentre. The curvature of the wavefront is significantly different from zero there and can be sufficiently well estimated for wavefront tomography. Generally speaking, in the present implementation, it is necessary that the receiver array records curved wavefronts. In that sense, the epicentres might also be located beyond the acquisition surface, however, they should not be arbitrarily far away. As already discussed previously, it is hard to determine what exactly marks an acquisition to be sufficiently dense. One could probably further reduce the number of receivers in example 4.3 to about 20 and the approach would still work. However, that would probably require larger optimization apertures and thus provide a less local estimation of the wavefront attributes, increasing the potential to average possible lateral variations. As a result one might obtain a smoother, less accurate velocity distribution. The similar trade-off is present for noisy data. Increasing the optimization aperture might be necessary to distinguish signals from noise and get wavefront attributes at all but this may also decrease the quality of the estimated wavefront attributes. The source excitation time estimation based on traveltime fitting requires global optimization apertures. Thus, for laterally heterogeneous media the values might be fairly biased.

If a refinement of the source excitation times is desired, multiple events from a similar region are necessary to ensure that a simultaneous inversion for improving the source excitation times and approximating the velocity distribution is successful. From our experience this approach leads to considerable improvements, especially regarding large errors in the initial source excitation times, see Table 1.

If these conditions are fulfilled, our workflow is a promising tool to localize passive seismic sources and simultaneously estimate the previously unknown subsurface velocities. Because of its built-in regularization and data enhancement facility it is quite robust and can deal with high noise levels and low-amplitude signals, respectively, as well as sparse data acquisitions. In our synthetic examples, the velocity distributions are approximated with a mean relative error of about 4 per cent considering absolute values. The sources, on the other hand, are localized with a maximum deviation in the order of the dominant wavelength of the signals. We have also exploited the potential of reverse time modelling, which does not explicitly dependent on errors in the source excitation time estimation. Thus, the sources are localized more accurately by reverse modelling than by wavefront tomography.

In order to further improve the results of the suggested approach, one could create a recursive scheme building on our workflow. The next step would involve an update of the source excitation times based on the improved source locations determined by reverse time modelling. Exploiting those new source excitation times another tomographic inversion to improve the velocity distribution could be carried out, followed by reverse time modelling to update the source locations again. Linking the two steps in such an iterative process combines the robustness of kinematic tomography and the independence of wavefield modelling from the tomography's possibly erroneous input data. In terms of computation, other optimization techniques might be investigated to improve and speed up the refinement of the source excitation times. Alternative curvature-based inversion schemes such as geometrical spreading focussing (Znak *et al.* 2018) could be investigated to further promote the workflow. Adapting the wavefront inversion concept to the characteristics of passive sources and including the tagging attribute (Bauer *et al.* 2019b) as additional information may further improve the inversion process. Knowing that equally tagged picks should focus in the respective hypocentre allows for reducing the model space and testing alternative objective functions. In fact, this feature of passive seismic events is equally interesting for diffractions in active seismic

Downloaded from https://academic.oup.com/gji/article-abstract/219/2/995/5539537 by Said Business School user on 23 September 2019

experiments (Bauer *et al.* 2017). Using the tags rather than curvatures, which are harder to estimate, along with the slope information should allow for a reliable, possibly more stable inversion (Bauer *et al.* 2019a). Furthermore, this approach would allow for considering body waves across a much wider range of epicentral distances. Our implementation of wavefront tomography builds on ray tracing. However, other techniques, for example based on Eikonal solvers, might be investigated in the future (Tavakoli *et al.* 2017; Sambolian *et al.* 2019). Despite the inherent challenges of a higher dimensionality of the search space, medium anisotropy can likewise be accounted for, if the ray tracing and reverse modelling engines are replaced by anisotropic counterparts. In this case, we foresee that a sufficiently large number of events needs to be considered to ensure that the trade-off between velocities, locations and source excitation times is as small as possible.

The presented synthetic 2-D data examples are considered here for demonstration purposes. Localization is an inherently 3-D problem. As the field data example has underlined, the workflow performs equivalently in 3-D. Obviously, further studies should investigate the source excitation time refinement in 3-D. A more involved issue might be to handle complicated source mechanisms. The approach obviously works best for explosive sources, however this is not a restriction. In general it is sufficient, if the waveforms are consistent within the optimization area. For instance, one could perform coherence analysis for the envelope of the seismic wavefield to resolve source radiation issues. Future work might also consider extended sources. A potential improvement of the inversion results might be obtained by including other phases, like *S* waves. Since they have the same source excitation times as the respective *P* waves and larger moveouts, that is larger curvatures, they might benefit the source excitation time estimation. Apart from that, the slight, but systematic underestimation of source excitation times is an issue which certainly needs further investigations.

7 CONCLUSION

We have presented a workflow to simultaneously determine source locations and seismic velocities from passive seismic data. It is largely automatic and independent of *a priori* information. The method requires a sufficiently dense receiver network nearby the epicentre of the considered event. Using coherence analysis, we can estimate wavefront attributes for the recorded signals, tag and thereby distinguish different events and obtain an initial guess of their respective source excitation times. Since this guess may display significant errors, a refinement is usually required. Such a refinement is achieved by adding the source excitation times to the unknowns in wavefront tomography. Provided that a reasonable starting guess is available, this approach corrects large deviations in the source excitation times and jointly delivers a velocity model that is consistent with the data. This model is then used in an imaging step, applying reverse time modelling to obtain an improved and probabilistic idea of the source locations based on the recorded waveform data. The presented synthetic data examples have underlined the robustness and efficiency of the workflow, delivering velocity estimations with a mean deviation of about 4 per cent and locations with maximum errors of about the dominant wavelength. We have obtained reliable results even from extremely noisy as well as sparsely sampled data because of the built-in data enhancement and regularization facility. Furthermore, we have used the method on field data from two local arrays to localize an earthquake without using *a priori* velocity information. The resulting location is close to the expected hypocentre and the retrieved velocities show a trend somewhat comparable to PREM.

Constructing a recursive scheme that iteratively updates the source excitation times for the tomography based on the event locations obtained from the imaging step might have strong potential. The demonstrated synthetic examples are simple in a sense that we have used explosive sources in an acoustic, isotropic medium, however, this is not a limitation inherent to the method. Other source mechanisms and additional phases may be included in further investigations.

ACKNOWLEDGEMENTS

The authors thank the Applied Seismic Group Hamburg and in particular Pavel Znak for fruitful and continuous discussion. Furthermore, the authors are grateful to Borhan Tavakoli and the editor Jean Virieux for constructive comments and feedback. This work has been supported by the sponsors of the Wave Inversion Technology (WIT) consortium and the Federal Ministry for Economic Affairs and Energy of Germany (BMWi, 03SX427B). The second author has been supported by a research fellowship of the German Research Foundation (DFG, SCHW 1870/1-1). Matlab and especially its optimization toolbox have been used for computations. The facilities of IRIS Data Services, and specifically the IRIS Data Management Center, have been used for access to waveforms, related metadata, and/or derived products shown in this study. IRIS Data Services are funded through the Seismological Facilities for the Advancement of Geoscience and EarthScope (SAGE) Proposal of the National Science Foundation under Cooperative Agreement EAR-1261681.

REFERENCES

Aki, K. & Lee, W., 1976. Determination of three-dimensional velocity anomalies under a seismic array using first P arrival times from local earthquakes: 1. A homogeneous initial model, *J. geophys. Res.,* **81**(23), 4381–4399.

Aki, K., Fehler, M. & Das, S., 1977. Source mechanism of volcanic tremor: fluid-driven crack models and their application to the 1963 Kilauea eruption, *J. Volc. Geotherm. Res.,* **2**(3), 259–287.

Anderson, M., Alvarado, P., Zandt, G. & Beck, S., 2007. Geometry and brittle deformation of the subducting Nazca Plate, Central Chile and Argentina, *Geophys. J. Int.,* **171**(1), 419–434.

Bauer, A., Schwarz, B. & Gajewski, D., 2017. Utilizing diffractions in wavefront tomography, *Geophysics,* **82**(2), R65–R73.

Bauer, A., Schwarz, B., Diekmann, L. & Gajewski, D., 2019a. Wavefront tomography with enforced diffraction focusing, in *Proceedings of the 81st EAGE Conference and Exhibition 2019,* EAGE.

Bauer, A., Schwarz, B., Werner, T. & Gajewski, D., 2019b. Unsupervised event identification and tagging for diffraction focusing, *Geophys. J. Int.,* **217**(3), 2165–2176.

Baykulov, M. & Gajewski, D., 2009. Prestack seismic data enhancement with partial common-reflection-surface (CRS) stack, *Geophysics,* **74**(3), V49–V58.

Beck, S. & Zandt, G., 2007. Lithospheric structure and deformation of the flat slab region of Argentina, International Federation of Digital Seismograph Networks. Dataset/Seismic Network. 10.7914/SN/ZL_2007.

Castle, R.J., 1994. A theory of normal moveout, *Geophysics,* **59**(6), 983–999.

De Boor, C., 1978. *A Practical Guide to Splines,* Springer.

Duveneck, E., 2004. Velocity model estimation with data-derived wavefront attributes, *Geophysics,* **69**(1), 265–274.

Dziewonski, A.M. & Anderson, D.L., 1981. Preliminary reference earth model, *Phys. Earth planet. Inter.,* **25**(4), 297–356.

Downloaded from https://academic.oup.com/gji/article-abstract/219/2/995/5539537 by Said Business School user on 23 September 2019

Eaton, J.P., 1970. HYPOLAYR, A computer program for determining hypocenters of local earthquakes in an Earth consisting of uniform flat layers over a half space, US Geological Survey, Open-File Report 69-85.

Eberhart-Phillips, D., 1986. Three-dimensional velocity structure in northern California Coast Ranges from inversion of local earthquake arrival times, *Bull. seism. Soc. Am.,* **76**(4), 1025–1052.

Ellsworth, W.L., 2013. Injection-induced earthquakes, *Science,* **341**(6142), 1225942.

Engdahl, E.R., van der Hilst, R. & Buland, R., 1998. Global teleseismic earthquake relocation with improved travel times and procedures for depth determination, *Bull. seism. Soc. Am.,* **88**(3), 722–743.

Farra, V. & Madariaga, R., 1987. Seismic waveform modeling in heterogeneous media by ray perturbation theory, *J. geophys. Res.: Solid Earth,* **92**(B3), 2697–2712.

Gajewski, D. & Tessmer, E., 2005. Reverse modelling for seismic event characterization, *Geophys. J. Int.,* **163**(1), 276–284.

Gajewski, D., Anikiev, D., Kashtan, B., Tessmer, E. & Vanelle, C., 2007. Localization of seismic events by diffraction stacking, in *Proceedings of the 77th SEG Meeting and Exposition 2007,* SEG.

Grigoli, F., Cesca, S., Amoroso, O., Emolo, A., Zollo, A. & Dahm, T., 2013. Automated seismic event location by waveform coherence analysis, *Geophys. J. Int.,* **196**(3), 1742–1753.

Hooke, R. & Jeeves, T.A., 1961. "Direct search" solution of numerical and statistical problems, *J. ACM (JACM),* **8**(2), 212–229.

Hubral, P., 1983. Computing true amplitude reflections in a laterally inhomogeneous Earth, *Geophysics,* **48**(8), 1051–1062.

International Seismological Centre, 2015. *On-line Bulletin,* http://www.isc.ac.uk, ISC, Thatcham, United Kingdom.

Ishii, M., Shearer, P.M., Houston, H. & Vidale, J.E., 2005. Extent, duration and speed of the 2004 Sumatra-Andaman earthquake imaged by the Hi-Net array, *Nature,* **435**(7044), 933.

Jäger, R., Mann, J., Höcht, G. & Hubral, P., 2001. Common-reflection-surface stack: Image and attributes, *Geophysics,* **66**(1), 97–109.

Kennett, B.L.N. & Engdahl, E.R., 1991. Traveltimes for global earthquake location and phase identification, *Geophys. J. Int.,* **105**(2), 429–465.

Kissling, E., Ellsworth, W., Eberhart-Phillips, D. & Kradolfer, U., 1994. Initial reference models in local earthquake tomography, *J. geophys. Res.: Solid Earth,* **99**(B10), 19635–19646.

Kissling, E., 1988. Geotomography with local earthquake data, *Rev. Geophys.,* **26**(4), 659–698.

Landa, E., Keydar, S. & Moser, T.J., 2010. Multifocusing revisited—inhomogeneous media and curved interfaces, *Geophys. Prospect.,* **58**(6), 925–938.

Langenbruch, C. & Zoback, M.D., 2016. How will induced seismicity in Oklahoma respond to decreased saltwater injection rates?, *Sci. Adv.,* **2**(11), e1601542.

Larmat, C., Montagner, J.-P., Fink, M., Capdeville, Y., Tourin, A. & Clévédé, E., 2006. Time-reversal imaging of seismic sources and application to the great Sumatra earthquake, *Geophys. Res. Lett.,* **33**(9).

Lee, W.H.K. & Lahr, J.C., 1972. HYPO71: a computer program for determining hypocenter, magnitude, and first motion pattern of local earthquakes, US Geological Survey, Open-File Report 72-224.

Li, L., Tan, J., Wood, D.A., Zhao, Z., Becker, D., Lyu, Q., Shu, B. & Chen, H., 2019. A review of the current status of induced seismicity monitoring for hydraulic fracturing in unconventional tight oil and gas reservoirs, *Fuel,* **242,** 195–210.

Lienert, B.R., Berg, E. & Frazer, L.N., 1986. HYPOCENTER: an earthquake location method using centered, scaled, and adaptively damped least squares, *Bull. seism. Soc. Am.,* **76**(3), 771–783.

Lienert, B.R. & Havskov, J., 1995. A computer program for locating earthquakes both locally and globally, *Seism. Res. Lett.,* **66**(5), 26–36.

Lomax, A., Virieux, J., Volant, P. & Berge-Thierry, C., 2000. Probabilistic earthquake location in 3D and layered models, in *Advances in Seismic Event Location,* pp. 101–134, Springer.

Mann, J., Jäger, R., Müller, T., Höcht, G. & Hubral, P., 1999. Common-reflection-surface stack—a real data example, *J. appl. Geophys.,* **42**(3-4), 301–318.

Maxwell, S.C. & Urbancic, T.I., 2001. The role of passive microseismic monitoring in the instrumented oil field, *Leading Edge,* **20**(6), 636–639.

Mayne, W.H., 1962. Common reflection point horizontal data stacking techniques, *Geophysics,* **27**(6), 927–938.

Paige, C.C. & Saunders, M.A., 1982. LSQR: an algorithm for sparse linear equations and sparse least squares, *ACM Trans. Math. Software (TOMS),* **8**(1), 43–71.

Rost, S. & Thomas, C., 2002. Array seismology: methods and applications, *Rev. Geophys.,* **40**(3), 2–1.

Rubinstein, J.L. & Mahani, A.B., 2015. Myths and facts on wastewater injection, hydraulic fracturing, enhanced oil recovery, and induced seismicity, *Seism. Res. Lett.,* **86**(4), 1060–1067.

Sambolian, S., Operto, S., Ribodetti, A., Tavakoli, F.B. & Virieux, J., 2019. Parsimonious slope tomography based on Eikonal solvers and the adjoint-state method, *Geophys. J. Int.,* **218**(1), 456–478.

Sandvol, E. & Brown, L., 2007. Slip-seismic lithospheric imaging of the Puna plateau, International Federation of Digital Seismograph Networks.

Schleicher, J., Tygel, M. & Hubral, P., 1993. Parabolic and hyperbolic paraxial two-point traveltimes in 3D media, *Geophys. Prospect.,* **41**(4), 495–513.

Schwarz, B., Vanelle, C., Gajewski, D. & Kashtan, B., 2014. Curvatures and inhomogeneities: an improved common-reflection-surface approach, *Geophysics,* **79**(5), S231–S240.

Schwarz, B., Bauer, A. & Gajewski, D., 2016. Passive seismic source localization via common-reflection-surface attributes, *Stud. Geophys. Geod.,* **60**(3), 531–546.

Segall, P. & Lu, S., 2015. Injection-induced seismicity: poroelastic and earthquake nucleation effects, *J. geophys. Res.: Solid Earth,* **120**(7), 5082–5103.

Shearer, P.M., 2019. *Introduction to Seismology,* Cambridge University Press.

Suckale, J., 2009. Induced seismicity in hydrocarbon fields, in *Advances in Geophysics,* Vol. **51,** pp. 55–106, Elsevier.

Sun, J., Xue, Z., Zhu, T., Fomel, S. & Nakata, N., 2016. Full-waveform inversion of passive seismic data for sources and velocities, in *Proceedings of the 86th SEG Meeting and Exposition 2016,* SEG.

Taner, M.T. & Koehler, F., 1969. Velocity spectra—digital computer derivation applications of velocity functions, *Geophysics,* **34**(6), 859–881.

Tarantola, A., 2005. *Inverse Problem Theory and Methods for Model Parameter Estimation,* SIAM.

Tavakoli, F.B., Operto, S., Ribodetti, A. & Virieux, J., 2017. Slope tomography based on Eikonal solvers and the adjoint-state method, *Geophys. J. Int.,* **209**(3), 1629–1647.

Thurber, C.H., 1992. Hypocenter-velocity structure coupling in local earthquake tomography, *Phys. Earth planet. Inter.,* **75**(1-3), 55–62.

Ursin, B., 1982. Quadratic wavefront and traveltime approximations in inhomogeneous layered media with curved interfaces, *Geophysics,* **47**(7), 1012–1021.

Wang, H. & Alkhalifah, T., 2018. Microseismic imaging using a source function independent full waveform inversion method, *Geophys. J. Int.,* **214**(1), 46–57.

Xie, Y. & Gajewski, D., 2017. 5-D interpolation with wave-front attributes, *Geophys. J. Int.,* **211**(2), 897–919.

Zhebel, O., Gajewski, D. & Vanelle, C., 2011. Localization of seismic events in 3D media by diffraction stacking, in *Proceedings of the 73rd EAGE Conference and Exhibition 2011,* EAGE.

Znak, P., Kashtan, B. & Gajewski, D., 2018. Velocity model building by geometrical spreading focusing, in *Proceedings of the 88th SEG Meeting and Exposition 2018,* SEG.

Downloaded from https://academic.oup.com/gji/article-abstract/219/2/995/5539537 by Said Business School user on 23 September 2019